https://ntrs.nasa.gov/search.jsp?R=20180007025 2020-02-10T19:09:23+00:00Z

69th International Astronautical Congress 2018, Bremen, Germany
This material is declared a work of the U.S. Government and is not subject to copyright protection in the United States.

IAC-18.C1.2.9
WIDE-FIELD INFRARED SURVEY TELESCOPE AND STARSHADE FORMATION FLYING DYNAMICS AT SUN-EARTH L2

Ariadna Farrés
NASA/GSFC Science Collaborator, University of Maryland Baltimore County,
ariadna.farresbasiana@nasa.gov

Cassandra M. Webster
WFIRST Flight Dynamics Lead, NASA Goddard Space Flight Center,
cassandra.webster@nasa.gov

Abstract

The formation flying of an occulter with a telescope at the Sun-Earth L2 (SEL2) Libration Point can be a challenging problem. A good knowledge of the Restricted Three Body Problem dynamics is required to understand how these two spacecraft interact with each other in the SEL2 unstable environment, and how other perturbations such as Solar Radiation Pressure (SRP) affect their mutual trajectories. This paper focuses on the transfer trajectories to achieve specific relative positions between two spacecraft as they fly in formation at SEL2, and analyzes the relevance of SRP in this formation, using the Wide-Field Infrared Survey Telescope (WFIRST) and the Starshade occulter as an example. Given that WFIRST and Starshade have very different area-to-mass ratios, SRP will affect their motion in different ways, and their relative position can be key to reduce the ΔV cost. In this paper we intend on providing an explanation on how the relative position between both spacecrafts affects the transfer ΔV from one observation to the other using dynamical system theory and Floquet modes.

1 INTRODUCTION

The Wide-Field InfraRed Survey Telescope (WFIRST), is a NASA observatory designed to explore dark energy, exoplanets, and infrared astrophysics[a]. It is planned for launch in 2025 and will orbit around the Sun-Earth L2 (SEL2) Libration Point. The telescope will have a primary mirror that is 2.4 meters in diameter, the same size as the Hubble Space Telescope's primary mirror, along with the Wide Field Instrument and the Coronagraph Instrument.

The Wide Field Instrument (WFI) will have a field of view that is 100 times greater than Hubble, capturing more of the sky with less observing time. With its large field of view, the WFI will be able to measure the light from a billion galaxies over the course of the mission lifetime, and will perform a microlensing survey of the inner Milky Way to find thousands of exoplanets.

The Coronagraph Instrument (CGI) will perform high contrast imaging and spectroscopy of dozens of individual nearby exoplanets. It will use internal occulting through different mirrors, lenses and masks to filter the starlight and image gas-giant planets and possibly super-Earths. Unfortunately, the ability to directly image another Earth-like planet will not be able to be done by the CGI alone as it does not have the contrasting power. However, the combination of the CGI with an external occulter, like Starshade, is believed to provide the high-contrast required to image Earth-sized planets in habitable zones of nearby stars.

Starshade is a 34 meter flower shaped occulter with razor-sharp petals that will be designed to redirect diffraction from a star's light (which will produce an undesirable glare) and create a shadow for WFIRST to observe an exoplanet using its CGI. Many researchers believe that Starshade along with the CGI on WFIRST would allow for a direct image of an Earth-like planet. Figure 1 shows the Telescope/Starshade observation concept [1].

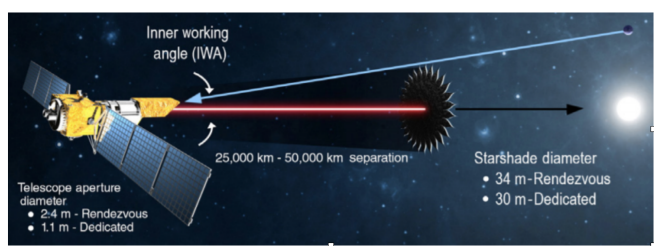

Fig. 1: Representation of the Telescope/Starshade concept.

Starshade will be launched several years after WFIRST, and will trail WFIRST in its Libation Point Orbit (LPO) at SEL2. After some time, Starshade will perform a maneuver to place itself in a different LPO, placed 37,000 km or more away from WFIRST. At this point, Starshade can begin slewing between WFIRST and a target star to attempt exoplanet observations. During the ob-

[a]WFIRST website `https://wfirst.gsfc.nasa.gov/`

This material is declared a work of the U.S. Government and is not subject to copyright protection in the United States.

servation campaign, WFIRST will remain in its baseline mission orbit, while Starshade will be offset from WFIRST's orbit, and must fly a specific trajectory to align itself with WFIRST in order to occult a set of pre-determined target stars given by a notional Design Reference Mission (DRM). Starshade plans to achieve all targeted observations over a time-span of 2 years.

The challenges of the WFIRST - Starshade formation alignments at SEL2 include: (a) achieving the observation locations with respect to WFIRST for each target star; (b) maintaining alignment during the observations while at a nominal 37,000 km away from each other; (c) while also managing the unstable SEL2 environment. Starshade will essentially operate like a hybrid solar sail and will undergo large perturbations due to Solar Radiation Pressure (SRP) which will affect the ΔV required for operations. Orbit maintenance maneuvers will also be required to keep both WFIRST and Starshade in the SEL2 environment.

In previous papers, we saw that the ΔV required for Starshade to slew from one observation to the other is highly dependent on the relative position between itself and WFIRST. The work in [7] shows how, taking the same DRM and changing its starting date by a month, would result in differences of up to 50 m/s in the total ΔV cost of the 2 year observation campaign. Moreover, transfer trajectories from one observation to another with the same slew time, resulted in very different ΔV maneuvers. Given that Starshade and WFIRST have different area-to-mass ratios this effect must be considered. In [6], the effect of SRP on the the total cost was explored. Again it was seen that the relative position between Starshade and WFIRST is important and had an impact on how SRP affected the total cost.

In this paper we continue analyzing the effects of SRP on the total ΔV cost of the WFIRST and Starshade formation flying mission concept. We will only focus on the transfer from one observation to the other, and also give some insight on the maintenance of this formation during an observation. Different DRMs will be considered to compare their impacts and see if certain configurations are more desired than others. As both spacecraft have different area-to-mass ratios, SRP plays an important role on the total ΔV, and must be taken into account. We will explore the effect on the total ΔV for different area-to-mass ratios for Starshade.

To start, an analysis considering the Restricted Three Body Problem (RTBP) including SRP as a model will be conducted. This will allow us to have a better understanding of Starshade and WFIRST coupled dynamics and how the invariant objects in the dynamical system play a role it this formation flying concept. A dynamical explanation using the Floquet modes describe the motion around a LPO will be performed. There we will be able to see how SRP affects the natural dynamics of both spacecrafts and how this impacts the total ΔV cost. Finally, this analysis will be extended in a higher fidelity model.

2 WFIRST - STARSHADE FORMATION

WFIRST's mission orbit is designed to meet its specific mission requirements, and is not to be adjusted to accommodate Starshade. While WFIRST is moving along its mission orbit, Starshade will follow a DRM, which includes a list of target stars and their observation times. During the observations Starshade must remain at a distance of 37,000 km away from WFIRST and maintain a specific geometry (WFIRST, Starshade and Star must be aligned) so that WFIRST's CGI can perform its observations. This distance can vary during the transfer of Starshade from one observation to the other, but it must meet the observations geometry at the beginning and end of each transfer.

Let us briefly describe the strategy that has been used to analyze the ΔV required for Starshade going from one observation to the other in this preliminary study. At the beginning of each simulation Starshade and WFIRST are assumed to be together, orbiting the same LPO at SEL2. At some point (set by the initial date, t_0, for the observation campaign) Starshade executes a maneuver to separate itself from WFIRST. At that point an initial ΔV is done to reach at the first observation point p_1 at time t_1. Once it reaches the first observation another ΔV is performed to guarantee that at the end of the observation, WFIRST and Starshade meet the required geometry. Once the first observation is finished, another ΔV is performed to reach the second observation p_2 at time t_2. This process is repeated until the end of the DRM. Figure 2 shows a schematic representation of this targeting scheme. Notice that this approach can be seen as a Bang-Bang control, where an initial ΔV maneuver is performed to accelerate Starshade to ensure that it reaches the observation location at a given time, and a second ΔV maneuver is performed in order to slow down Starshade and guarantee that at the end of the observation time the relative positions is maintained. To find each of the ΔV maneuvers, a simple differential corrector with three conditions and three unknowns is required.

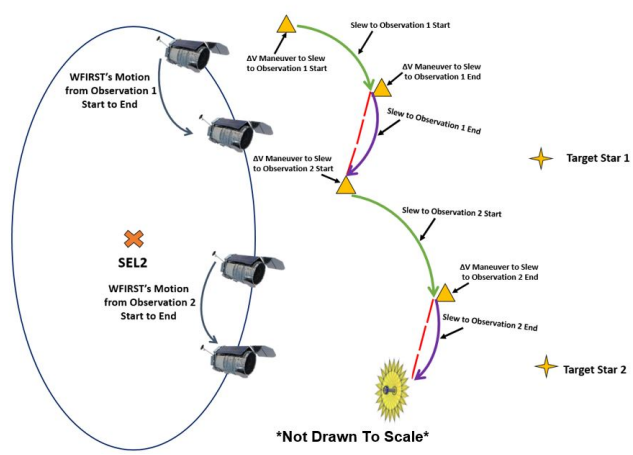

Fig. 2: Schematic representation of the Starshade targeting method.

We recall that in this paper we do not focus on keeping the relative distance of 37,000 km and alignment configuration between WFIRST - Starshade - Star during the observations, we just require that this configuration is met at the beginning and at the end of each observation. However, in some cases, we will compute how the relative distance between WFIRST - Starshade and their alignment with the stars varies during an observation. By looking

This material is declared a work of the U.S. Government and is not subject to copyright protection in the United States.

at how this alignment varies during the observations, we can see how necessary an active control will be in order to maintain the correct alignment.

3 FORCE MODELS

The main forces that affect the motion of WFIRST and Starshade in the vicinity of SEL2 are the gravitational pull of Earth and Sun. The perturbation of the other planets in the solar system and the Moon are relevant but do not have a large impact on the qualitative behavior of the trajectory. Nevertheless, as Starshade and WFIRST have very different area-to-mass ratios, SRP will affect their motion in different ways and must be included in the simulations. As it will be seen in this paper, the differences between the two spacecrafts' area-to-mass ratios can have a drastic effect on the the total cost of their formation flying.

3.1 Restricted Three Body Problem

A simple model to describe the motion of WFIRST and Starshade in the Earth - Sun vicinity is the classical Circular RTBP including the effect due to SRP.

The Circular RTBP assumes Earth and Sun to be point masses moving around their common center of mass in a circular way due to their mutual gravitational attraction. The spacecraft on the other hand, is a mass-less particle that does not affect the motion of the two primaries but is affected by their gravitational attraction as well as the SRP.

It is common to consider a rotating reference frame with the origin at the center of mass of the Earth - Sun system, where Earth and Sun are fixed on the x-axis (with its positive side pointing towards the Earth), the z-axis is perpendicular to the ecliptic plane and the y-axis completes an orthogonal positive oriented reference system (see Fig.3). The units of mass, distance and time, are normalized so the total mass of the system is 1, the Earth - Sun distance is 1 and the period of one Earth - Sun revolution is 2π. With these assumptions, the equations of motion are given by:

$$\ddot{x} - 2\dot{y} = \frac{\partial \Omega}{\partial x} + a_x,\ \ddot{y} + 2\dot{x} = \frac{\partial \Omega}{\partial y} + a_y,\ \ddot{z} = \frac{\partial \Omega}{\partial z} + a_z, \quad (1)$$

where $\Omega(x, y, z) = \frac{1}{2}(x^2 + y^2) + \frac{(1-\mu)}{r_{ps}} + \frac{\mu}{r_{pe}}$, with $r_{ps} = \sqrt{(x+\mu)^2 + y^2 + z^2}$ and $r_{pe} = \sqrt{(x+\mu-1)^2 + y^2 + z^2}$ the Sun-sail and Earth-sail distances respectively, and $\mathbf{a} = (a_x, a_y, a_z)$ is the SRP acceleration.

3.2 Point Mass Ephemeris model

In order to validate the results presented here, simulations with a higher fidelity model have been performed. These simulations have been done using the AGI software Systems Tool Kit (STK) [b].

[b] STK http://www.agi.com/products/engineering-tools

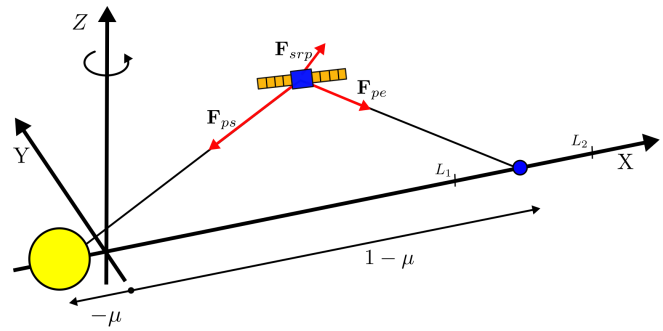

Fig. 3: Schematic representation of the RTBP.

The force model for these simulations considers the spacecraft as a mass-less particle that is affected by the gravitational attraction of Sun, Earth, Moon and Jupiter, and SRP. The four main bodies are considered to be point masses following their true motion given by JPL DE421 ephemeris. [c]

Let $\mathbf{R} = (x, y, z)$ be the spacecraft's position, $\mathbf{R}_i = (x_i, y_i, z_i)$ be the position of Sun, Earth, Moon and Jupiter with respect to the Solar system barycenter ($i = S, E, M$ and J respectively) and m_S, m_E, m_M and m_J their respective masses. Then, the equations of motion are given by:

$$\ddot{\mathbf{R}}_{S,sc} = -Gm_S \frac{\mathbf{R}_{S,sc}}{R^3_{S,sc}} + \sum_{i=E,M,J} \left[Gm_i \left(\frac{\mathbf{R}_{i,sc}}{R^3_{i,sc}} - \frac{\mathbf{R}_i}{R^3_i} \right) \right] + \mathbf{a}_{srp}, \quad (2)$$

where, $\mathbf{R}_{S,sc}, \mathbf{R}_{E,sc}, \mathbf{R}_{M,sc}, \mathbf{R}_{J,sc}$ are the Sun-spacecraft, Earth-spacecraft, Moon-spacecraft and Jupiter-spacecraft directions respectively, and $\mathbf{a}_{srp}$ and represents the SRP acceleration.

3.3 Solar Radiation Pressure

Solar Radiation Pressure is the acceleration caused by the exchange in momenta between the solar photons and the spacecraft's surface. The incident photons will be absorbed and reflected by the surface of the spacecraft, where the rates of absorption (ρ_a) and reflection (ρ_s, ρ_d) depend on the properties of the surface material (Fig. 4). Hence, the total acceleration due to SRP will vary depending on the shape of the spacecraft, the reflectivity properties of the materials, and its relative orientation with respect to the Sun-spacecraft line. Despite being small compared to the gravitational attraction of the main bodies in the system, SRP plays an important role in the dynamics of LPO [10, 11] and needs to be considered.

In the literature we find several ways to model this effect [3, 5, 8], which vary depending on the required level of fidelity. In this paper we have used the cannonball model for WFIRST's motion and define its reference orbit. This study does not analyze how SRP affects WFIRST's trajectory and station-keeping. While for Starshade we use both the cannonball and the flat plate model.

[c] SPICE Toolkit: https://naif.jpl.nasa.gov/naif/toolkit.html

This material is declared a work of the U.S. Government and is not subject to copyright protection in the United States.

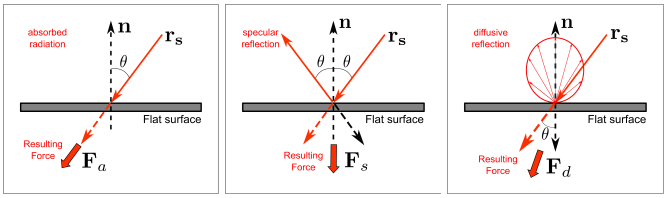

Fig. 4: Schematic representation of the resulting forces due to absorption (left), specular reflection (middle) and diffusive reflection (right) on a flat surface.

3.3.1 Cannonball model

The cannonball model is the simplest and most common way to model SRP. In this model, the force direction is always along the Sun-spacecraft direction ($\mathbf{r}_s$) and its magnitude depends on the area-to-mass ratio (A_{sat}/m_{sat}) and an estimated reflectivity coefficient $C_r \in [1, 2]$:

$$\mathbf{a}_{srp} = -\frac{P_{srp} C_r A_{sat}}{m_{sat}} \mathbf{r_s}, \tag{3}$$

where $P_{srp} = P_0(R_0/R_{sun})^2$ is the radiation pressure at a distance R_{sun} from the Sun (where $P_0 = 4.57 \times 10^{-6}$ N is the SRP at $R_0 = 1$ AU from the Sun). The C_r coefficient is hard to predict as it depends on the spacecraft's reflectivity properties. For instance, $C_r = 1$ corresponds to the case where all the Sun-light is absorbed, while $C_r = 2$ indicates that all the Sun-light is reflected [3].

3.3.2 Flat plate model

With this model, the spacecraft's shape is approximated by a flat plate, and the total force depends on the rate of absorbed (ρ_a) and reflected (ρ_s) solar photons. Hence, the total force due to SRP is the sum of the force produced by: the absorbed photons ($\mathbf{F_a} = P_{srp} A \langle \mathbf{n}, \mathbf{r_s} \rangle \mathbf{r_s}$) and the reflected photons ($\mathbf{F}_s = 2P_{srp} A \langle \mathbf{n}, \mathbf{r_s} \rangle^2 \mathbf{n}$). Notice that only specular reflection has been considered. In order to have a more accurate approximation, diffusive reflection should also be considered, but this is a preliminary analysis and diffusive reflection is usually very small.

Given that the photons are either absorbed or reflected, the coefficients (ρ_a, ρ_s) must satisfy $\rho_a + \rho_s = 1$, and the total SRP acceleration is given by:

$$\mathbf{a}_{srp} = -\frac{P_{srp} A}{m_{sat}} \langle \mathbf{n}, \mathbf{r_s} \rangle \left[(1 - \rho_s) \mathbf{r_s} + 2\rho_s \langle \mathbf{n}, \mathbf{r_s} \rangle \mathbf{n} \right], \tag{4}$$

where $\mathbf{r}_s$ is the normalized spacecraft-Sun direction and $\mathbf{n}$ is the normal direction to the flat surface pointing away from the Sun.

3.3.3 Normalized SRP acceleration values

Notice that P_{srp} depends on the inverse of the Sun-spacecraft distance in the same way as the Sun's gravitational attraction. Hence it is common to define the parameter q_{srp} as the ratio between the SRP acceleration ($P_{srp} A_{sat}/m_{sat}$) and the acceleration due to the Sun's gravity ($G m_s / r_{ps}$).

Using this parameter Eqs. 3 and 4 can be rewritten as:

$$\mathbf{a}_{srp} = -q_{srp} C_r \frac{1-\mu}{r_{ps}^2} \mathbf{r}_s, \tag{5}$$

$$\mathbf{a}_{srp} = -q_{srp} \frac{1-\mu}{r_{ps}^2} \langle \mathbf{n}, \mathbf{r_s} \rangle \left[(1 - \rho_s) \mathbf{r_s} + 2\rho_s \langle \mathbf{n}, \mathbf{r_s} \rangle \mathbf{n} \right] \tag{6}$$

where $q_{srp} = K_s(A_{sat}/m_{sat})$ for $K_s = (P_0 R_0^2 / G m_{sun}) = 7.7065 \times 10^{-4}$ when A_{sat} and m_{sat} are given in m^2 and kg, respectively.

Notice that when the plate is perpendicular to the Sun-spacecraft direction (i.e. $\mathbf{n} \parallel \mathbf{r}_s$) Eq. 5 and Eq. 6 are the same for $C_r = 1 + \rho_s$. Moreover, in this case, we can merge the SRP acceleration with the Solar gravitational attraction in Eq.1 and rewrite $\Omega(x, y, z)$ as $\widetilde{\Omega}(x, y, z) = \frac{1}{2}(x^2 + y^2) + \frac{(1 - q_{srp} C_r)(1-\mu)}{r_{ps}} + \frac{\mu}{r_{pe}}$.

In this paper, for WFIRST, an estimated area-to-mass ratio of 0.06 m$^2/kg$ has been assumed and $C_r = 1.25$, as during most of the mission the solar panels will be pointing towards the Sun. On the other hand, for Starshade, an area of 804m^2 (corresponding to a 32 m diameter) and a total mass between 2700 - 3500 kg has been assumed. Figure 5 shows the variation of the normalized SRP acceleration rate, $q_{srp} C_r$, for different reflectivity values $\rho_s = 0.1, \ldots, 0.9$, which varies between 4.7×10^{-4} and 1.9×10^{-4}. For comparison, note that for WFIRST $q_{srp} Cr = 5.7842 \times 10^{-6}$, having a difference of almost two orders of magnitude between the SRP acceleration experienced by Starshade and WFIRST.

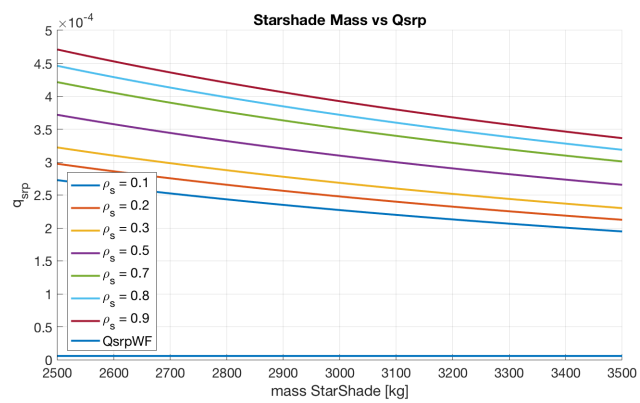

Fig. 5: Relation between Starshade mass and the normalized SRP acceleration $q_{srp}(1 + \rho_s)$ for an 804 m^2 area.

4 Solar Radiation Pressure effects on the RTBP dynamics

It is well known that when we include the SRP effect on the RTBP, the five equilibrium points of the system are displaced towards the Sun [9, 10]. The same happens with the different families of periodic and quasi-periodic orbits in the system. For small q_{srp} values the qualitative behavior of the system is the same.

This material is declared a work of the U.S. Government and is not subject to copyright protection in the United States.

Note that for simplicity, in this section we will consider $C_r = 1$ and refer always to the normalized SRP acceleration as q_{srp}.

Table 1 shows the position of the SEL2 point for different q_{srp} values. It can be seen that there is a difference of more than 8,000 km between the location of the displaced SEL2 for Starshade ($q_{srp} \approx 2 \times 10^{-4}$) and WFIRST ($q_{srp} \approx= 5.0 \times 10^{-6}$).

Table 1: Location of the displaced L_2 point as a function of q_{srp}.

q_{srp}	L_2 (AU)	L_2 (km)
0.0	1.01007520e+00	151105099.1699
5.0e-06	1.01007464e+00	151105016.6238
1.0e-04	1.01006417e+00	151103449.9413
5.0e-04	1.01002031e+00	151096888.5529

Figure 6 (top) shows the XZ components of the Northern Halo orbits family that intersect the Poincaré section $\{Y = 0,\ \dot{Y} > 0\}$. Note that each point on the plot corresponds to one periodic orbit. In the plot we can see how the periodic orbits move towards the Sun as q_{srp} increases. Figure 6 (bottom) shows the relation between the Z amplitude of these Halo orbits on the Poincaré section and their orbital period. Here we can see a maximum distance of $\approx 10,000$ km in the Poincaré section and a difference of 1 day in the orbital period between the two most extreme cases.

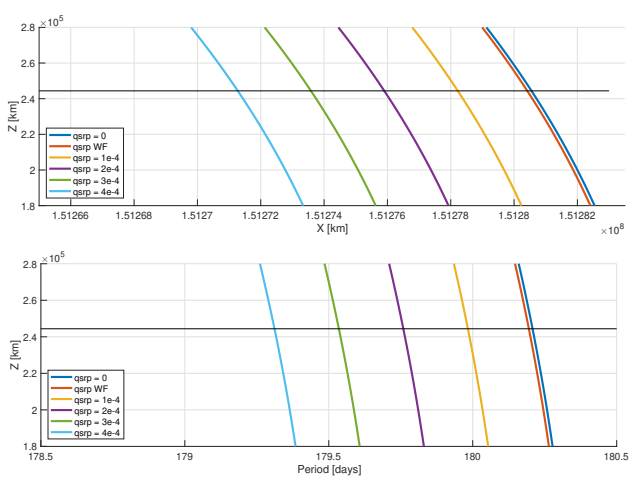

Fig. 6: For different q_{srp} values, family of Halo orbits where $Z_{max} \in [120000, 220000]$ km. Top: Z vs X on the $Y = 0$ Poincaré section, Bottom: Z vs T the orbits period.

This means that the natural dynamics for each spacecraft in the SEL2 environment will be different as each one of them will be governed by the linear and non-linear dynamics of different Halo orbits, that are displaced from each other and have different orbital periods. By imposing the requirement that Starshade and WFIRST maintain a certain relative distance, we are forcing Starshade to follow an unnatural path, which can increase the ΔV to do operations.

5 Dynamics around a Halo orbit

To fix notation, let ϕ be the flow associated to the equations of motion (Eq. 1). Where, $\phi_\tau(x_0)$ is the state of the spacecraft at time $t = \tau$ for an initial state $x_0 \in \mathbb{R}^6$, and $A(\tau) = D_x\phi_\tau(x_0)$ is the first order variational of $\phi_\tau(x_0)$ with respect to the initial condition, x_0.

The local behavior around a periodic orbit, can be described through the study of the eigenvalues and eigenvectors of the state transition matrix $A(T)$, where T is the period of the orbit. One can check that for all the Halo orbits considered here the eigenvalues ($\lambda_{1,\ldots,6}$) of $A(T)$ always satisfy: $\lambda_1 > 1, \lambda_2 < 1, \lambda_3 = \bar{\lambda}_4$ (have modulus one), and $\lambda_5 = \lambda_6 = 1$. These three pairs of eigenvalues and their associated eigenvectors have the following geometrical meaning [12]:

- The first pair (λ_1, λ_2), verify $\lambda_1 \cdot \lambda_2 = 1$, and are related to the hyperbolic character of the orbit. The value λ_1 is the largest in absolute value, and is related to the unstable eigenvalue $e_1(0)$, the most expanding direction. On the other hand, λ_2 is the smallest in absolute value, and is related to the stable eigenvalue $e_2(0)$, the most contracting direction. The motion on the plane generated by the propagation of these two directions along the orbit is a saddle.
- The second pair (λ_3, λ_4) are complex conjugate eigenvalues of modulus 1. The motion on the plane spanned by $e_3(0)$ and $e_4(0)$ (the real and imaginary parts of the eigenvectors associated to λ_3, λ_4) along the orbit is a rotation of angle $\Gamma = \arctan\left(\frac{Im(\lambda_3)}{Re(\lambda_3)}\right)$ along the orbit.
- The third couple $(\lambda_5, \lambda_6) = (1, 1)$, is associated to the neutral directions. The state transition matrix $A(T)$ only has one eigenvector with eigenvalue equal to 1, the tangent vector to the orbit, that we call $e_5(0)$. The other eigenvalue is associated to variations of the period, or any other variable that parameterise the family of periodic orbits.

The functions $e_i(\tau) = A(\tau) \cdot e_i(0)$, $i = 1, \ldots, 6$, represent the local approximations of the unstable, stable, center invariant manifolds along the orbit. Moreover, they help us describe the natural dynamics in the vicinity of a periodic orbit. From these six functions one can derive the so called *Floquet modes* $\bar{e}_i(\tau)$, $i = 1, \ldots, 6$, six T-periodic functions that define a periodic reference frame around a periodic orbit. The main advantage of the Floquet modes is that they are periodic functions and can be spanned as a Fourier series and stored by their Fourier coefficients. For further details see [12].

In the Floquet modes reference frame $\{\bar{e}_1(\tau), \ldots, \bar{e}_6(\tau)\}$, the dynamics around a Halo orbit is simple: on the planes generated by $\bar{e}_1(\tau), \bar{e}_2(\tau)$ the motion is a saddle, having the trajectory escape with an exponential rate along the unstable direction ($\bar{e}_1(\tau)$); on the planes generated by $\bar{e}_3(\tau), \bar{e}_4(\tau)$ the dynamics consists of a rotation around the periodic orbit; and on the planes generated by $\bar{e}_5(\tau), \bar{e}_6(\tau)$ the dynamics is neutral. Figure 7 shows a schematic representation of the linear dynamics around the Halo orbit using

This material is declared a work of the U.S. Government and is not subject to copyright protection in the United States.

this reference frame, where the origin of coordinates corresponds to the periodic orbit. Note that this reference frame not only allows us to have a good description of the motion on the spacecraft close to a Halo orbit, but can also be used to make decisions on station-keeping maneuvers [13, 15, 14].

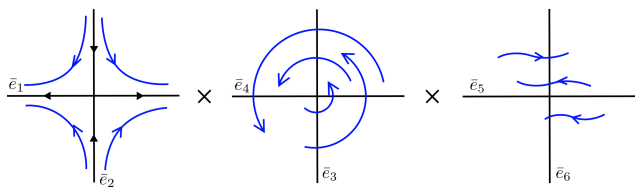

Fig. 7: Schematic representation of the linear dynamics around a Halo orbit using the Floquet modes $\bar{e}_i(\tau)$.

Let us now illustrate how the Floquet modes can help us describe the dynamics close to Halo orbits and the performance of station-keeping maneuvers. Figure 8 shows the motion of a spacecraft orbiting close to a Halo orbit. The orbit on the left plot, no control is applied and the trajectory escapes. While the orbit on the right plot, station-keeping maneuvers ever 42 days are applied and the spacecraft completes 3 orbital periods (in this example $q_{srp} = 0$).

The station-keeping strategy that has been used in this example is the *two plane crossing*, where the required ΔV is computed to ensure that after the second time the trajectory reaches the $\{y = 0\}$ plane, then $\dot{x} = 0$ (the v_x component of the velocity vector is zero). This ensures that the trajectory is close to a periodic orbit and continues to orbit. This is a simple station-keeping approach that has been used in the past to orbit around LPOs.

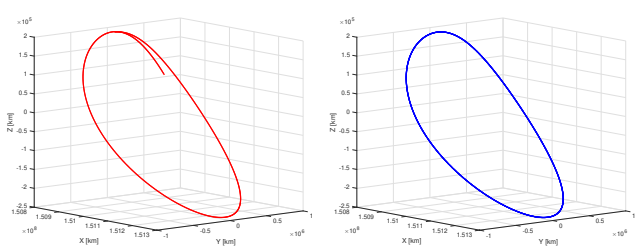

Fig. 8: Satellite's trajectory around a Halo orbit for $q_{srp} = 0$ in the RTBP. Left: No station-keeping; Right: Station-keeping every 42 days.

Let us now look at the projection of these two trajectories in the Floquet modes reference frame (Fig. 9). The top plot in Fig. 9 shows the projection of the uncontrolled trajectory. Notice how the trajectory escapes along the unstable direction as expected (left), and rotates around the periodic fixed point representing the periodic orbit (middle). Once the trajectory is far from the periodic orbit, the linear approximation is not good enough and the trajectory can be seen as a straight line. The bottom plot in Fig. 9 shows the controlled trajectory, each ΔV maneuver can be seen as a jump in the phase space (i.e. an instantaneous change of the velocity vector). If we look at the projection of the trajectory in the saddle plane ($\{\bar{e}_1, \bar{e}_2\}$), we can see how the trajectory escapes along the unstable direction; and each time a maneuver is performed it comes close to the stable direction. This ensures that the trajectory will come close to the periodic orbit and satisfy the $v_x = 0$ constraint. The projection of the trajectory in the center directions ($\{\bar{e}_3, \bar{e}_4\}$) is a rotation, and each time a ΔV maneuver is performed the phase and size of the rotation is changed. In some cases it can be interesting to observe the trajectories in this projection to unsure that they remain close to the reference Halo orbit. Finally, the projection in the neutral directions ($\{\bar{e}_5, \bar{e}_6\}$) is less relevant but it can be understood as a small drift along the nearby periodic orbits in the family.

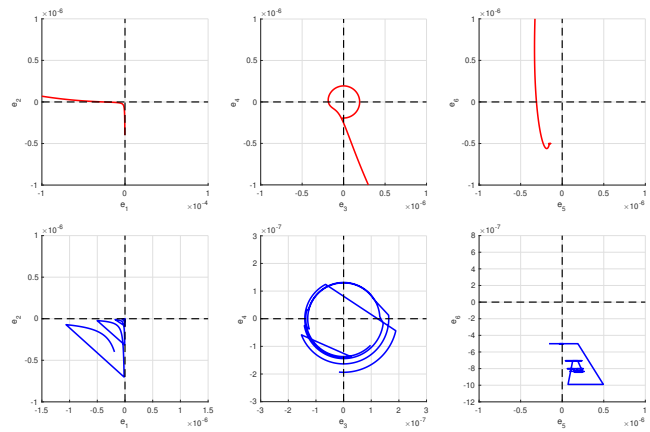

Fig. 9: Projection of the spacecraft's trajectory for $q_{srp} = 0$ on the Floquet mode frame. Top: No station-keeping; Bottom: Station-keeping every 42 days.

With this example we want to show the importance of understanding the dynamics around a Halo orbit. Notice that despite not taking the dynamics into account when planning the station-keeping maneuvers, the natural way to control the orbit is to perform ΔV maneuvers that bring the spacecraft close to the stable manifold. This information can be used to improve the decision on initial guesses for station-keeping.

5.1 Dynamics for different SRP effects

Let us briefly discuss how different SRP affects the trajectory and control along a Halo orbit. This will help us understand the coupled motion between Starshade and WFIRST. As we have seen in Section 4 the location of the Halo orbits is displaced when the SRP is included in the model. This means that the natural Halo orbit and its stable and unstable manifolds governing the motion of the spacecraft are displaced.

In this example we take again as reference frame the associated Floquet modes from the Halo orbit in Fig. 8 ($q_{srp} = 0$) and perform the same simulations as before: one uncontrolled trajectory and another applying the two plane crossing control every 42 days. The initial condition for the spacecraft states are the same as in the previous simulations, the only difference is that here for both simulations $q_{srp} = 10^{-5}$. Figure 10 shows the projection of these two trajectories in the Floquet reference frame. The top plot corresponds to the uncontrolled trajectory, while the bottom plot corresponds to the controlled trajectory.

Both plots in Fig. 10 show the same behavior as in Fig. 9, but now the invariant manifolds that drive the spacecraft's trajectory have

This material is declared a work of the U.S. Government and is not subject to copyright protection in the United States.

been shifted. This shift of the invariant manifolds can be clearly seen on the saddle projection of the trajectory shown in the left plots of Fig. 10.

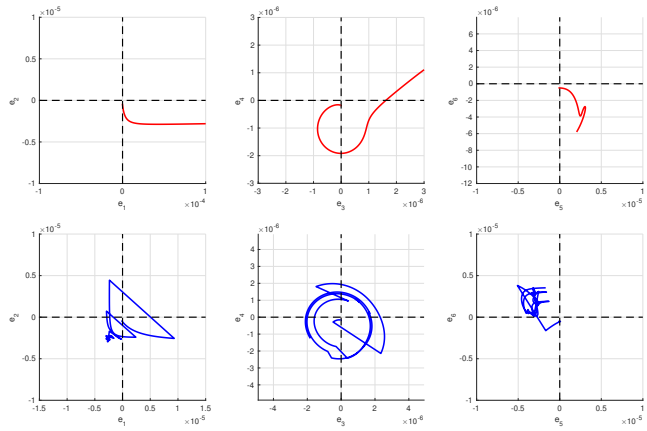

Fig. 10: Projection of the spacecraft's trajectory for $q_{srp} = 10^{-5}$ on the Floquet mode frame. Top: No station-keeping; Bottom: Station-keeping every 42 days.

6 WFIRST-STARSHADE FORMATION FLYING

Let us now focus on the formation flying of WFIRST and the Starshade at SEL2. The strategy followed to compute the required maneuvers to slew from one observation to the other has been described in Section 2, where ΔV's are performed at the start and end of each observation in order to reach a specific location at the initial and final time of an observation.

In this paper we want to analyze the importance of SRP in this formation flying concept, given that both spacecrafts have very different area-to-mass ratios (i.e. different q_{srp} coefficients). In Section 4 we have seen how much the families of Halo orbits are displaced for the different q_{srp} values, and in Section 5 how this shift of the Halo orbits location can affect the control of a spacecraft around a Halo orbit. In the case of Starshade and WFIRST, the families of Halo orbits associated to each spacecraft, and their stable and unstable manifolds, are more than 10000 km apart, hence the instability of the system affects both spacecrafts, as they fly in formation, in very different ways.

We start by performing some test cases, where we show how the location of the observations in the phase space has an impact on the total ΔV. These test cases have been analyzed in the RTBP framework, where we analyze the effect of changing q_{srp} and the reflectivity coefficient C_r, ρ_s affects the total ΔV. Simulations using both the cannonball and the flat plate models are performed. Finally a 48 observation DRM provided by the JPL Starshade group is analyzed. For this DRM the estimated area-to-mass ratios for WFIRST and Starshade are considered and only the effect of changing the reflectivity properties of Starshade is studied. This 48 observation DRM case is analyzed in the RTBP reference and of a high fidelity force model using STK.

6.1 Test DRM with 10 Observations

As we have mentioned throughout this paper, we want to show how SRP affects the ΔV budget. We also wanted to investigate how different relative WFIRST-Starshade positions have different effects on changes in the SRP coefficient q_{srp}.

Three different DRMs with 10 observations each, for a time-line of 6 months, have been analyzed. Most of these observations might not belong to a relevant star, as they have been chosen for test purposes, but they are within WFIRST's field of view (i.e. recall that the WFIRST's observing zone is $54°$ to $126°$ off the Sun-line). The first set of 10 observations (DRMT) are all within an offset Sun-line angle $\gamma \in [60°, 80°]$ (towards the Sun view), the second set of 10 observations (DRMA) all the observations satisfy $\gamma \in [100°, 120°]$ (away from the Sun view) and finally for the third set of 10 observations (DRMM) the angle γ is within the observing zone. Figure 11 shows Starshade's trajectory relative to WFIRST for each of the DRM's (from left to right DRMT, DRMA, DRMM), where in each plot the red points correspond each of the observations.

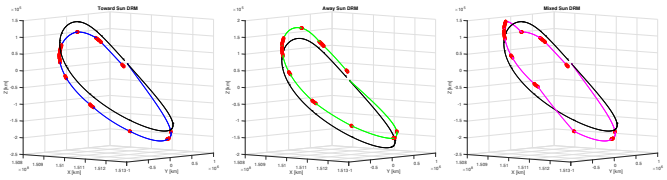

Fig. 11: Trajectory of Different DRM options.

As we saw in section 3.3.3, depending on the final area-to-mass ratios, the SRP coefficients can be very different. In these test cases, we have taken normalized numbers. For WFIRST we have considered for all the simulations $q_{srp} = 5 \times 10^{-6}$ and $C_r = 2$. While for Starshade, we have performed simulations using the cannonball model, with $q_{srp} = 5 \times 10^{-6}, 1 \times 10^{-4}, 2 \times 10^{-4}$ and 3×10^{-4} and $C_r = 2$, and simulations using the plate model with $q_{srp} = 2 \times 10^{-4}$ and $\rho_s = 0, 0.5$ and 1.0. These different cases will help us understand how Starshade's area-to-mass ratio and reflectivity properties affect the ΔV.

6.1.1 Simulations using cannonball for SRP

Table 2 shows the total ΔV for each of the three test DRM's and different q_{srp} values. Here we can see that DRMM is almost two times more expensive than DRMT and DRMA, hence, concentrating all the observations in the same region can help reduce the overall cost. Looking at the results for case `Q01` (where Starshade and WFIRST have the same q_{srp}) there is not much of a difference between DRMT and DRMA, but as q_{srp} increases, we see how the total ΔV for DRMT decreases, while it increases for DRMA. In order to understand why changing SRP has this effect on DRMT and DRMA we must look at the projection of the trajectories in the saddle and center planes.

Figure 12 shows the projection of the different trajectories simulated in the saddle and center planes ($\{e_1, e_2\}$, $\{e_3, e_4\}$ respectively) for DRMT (top) and DRMA (bottom), and Fig. 13 shows

This material is declared a work of the U.S. Government and is not subject to copyright protection in the United States.

the same projections for DRMM. In all of the plots, the color corresponds to a different q_{srp} value.

Table 2: Total ΔV for the different DRM's changing the SRP coefficients q_{srp} in the cannonball model.

id	q_{srp}	C_r	DRMT [m/s]	DRMA [m/s]	DRMM [m/s]
Q01	5×10^{-6}	2.0	181.07	180.53	337.04
Q02	1×10^{-4}	2.0	179.46	183.30	336.68
Q03	2×10^{-4}	2.0	178.82	187.20	337.25
Q04	3×10^{-4}	2.0	179.35	192.11	338.91

In order to understand these plots, let us recall that as discussed in Section 4, changes in the SRP coefficients q_{srp} will drift the natural Halo orbit in the system. Hence for each of the cases analyzed here (Q01, Q02, Q03 and Q04) the natural Halo orbit and the saddle and center location for each case are shifted, affecting Starshade's trajectory in a different way.

Given that increasing q_{srp} drifts the Halo orbits towards the Sun (Fig. 6), it is natural that the overall effect of increasing q_{srp} is completely different comparing DRMT with DRMA. On the top of Fig. 12 (DRMT) case we can appreciate how the saddle behavior of the different slew trajectories changes as q_{srp} increases. In this case the center of the saddle comes towards the observations, having smaller drifts in the trajectory reducing the overall cost. On the other hand, for DRMA case (Fig. 12 bottom) the center of the saddle plane is displaced away from the observations as q_{srp} increases, resulting in a more unstable environment making the total cost, to meet the observations requirements, increase. In both cases we can appreciate a small drift in the location of the center of rotation on the $\{e_3, e_4\}$ projection.

Finally, this drift can also be seen in the projections of DRMM on the saddle and center planes (Fig. 13), where Table 2 shows a small increase on the total ΔV (less relevant than for DRMA). In this case the observation locations are on both sides of the saddle, so drifting its location increases the ΔV on one side and decreases on the other side, compensating the total cost.

6.1.2 Simulations using Plate Model for SRP

Table 3 shows the total ΔV for each of the three test DRM's and $q_{srp} = 2 \times 10^{-4}$ and different ρ_s values. Recall that ρ_s is related to the reflectivity properties of the Starshade material, and that changing ρ_s not only affects the SRP acceleration magnitude but also its direction (see Section 3.3). Notice how again, the total ΔV for DRMM is almost twice the ΔV required for DRMT and DRMA. Notice that increasing ρ_s can also be related to increasing the total SRP acceleration. Hence for DRMA and DRMM we can see how the total ΔV increases with ρ_s. Again, in order to understand and visualize the effect of changing ρ_s in the SRP acceleration we must look at the projection of the trajectories in the saddle and center planes.

Figure 14 shows the projection of the different trajectories simulated on the saddle and center planes ($\{e1, e2\}, \{e3, e4\}$ respectively) for DRMT (top), DRMA (middle) and DRMM (bottom). Now changing ρ_s does not drastically move the location of the saddle, so small changes can be seen for each of the DRM's in the plots. It would be interesting to perform a more detailed study on how Starshade's attitude affects the required ΔV for transfer from one observation to the other. We recall that for all the simulations here, Starshade is perpendicular to the Sun-line during transfers and perpendicular to the WFIRST-Starshade line during observations, but variations to Starshade's attitude during the transfer from one observation to the other can be made and might have an impact on the ΔV cost.

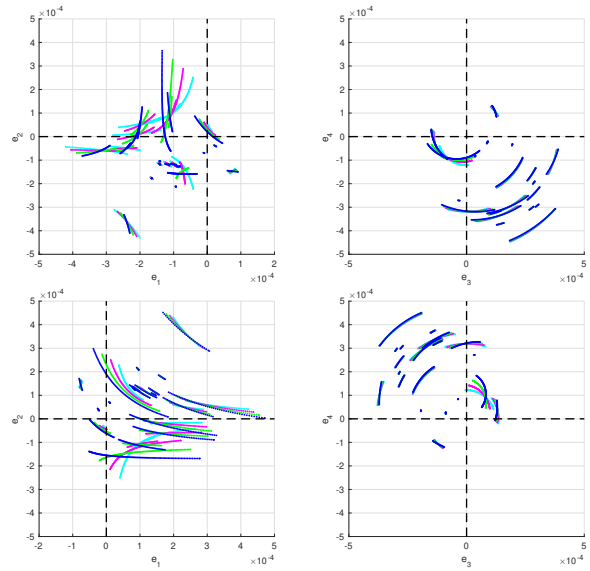

Fig. 12: Projection of Starshade trajectory on the saddle plane $\{e_1, e_2\}$ (left) and center plane $\{e_3, e_4\}$ (right) for cases Q01 cyan, Q02 magenta, Q03 green, Q04 blue. Top: DRMT trajectory, Bottom: DRMA trajectory.

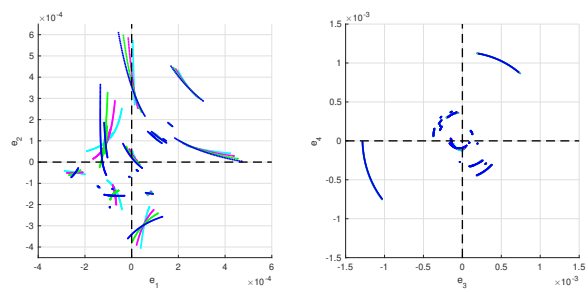

Fig. 13: Projection of Starshade trajectory for DRMM on the saddle plane $\{e_1, e_2\}$ (left) and center plane $\{e_3, e_4\}$ (right) for cases Q01 cyan, Q02 magenta, Q03 green, Q04 blue.

Table 3: Total ΔV for the different DRM's changing the SRP coefficients ρ_s in the plate model.

id	q_{srp}	ρ_s	DRMT [m/s]	DRMA [m/s]	DRMM [m/s]
R01	2×10^{-4}	0.0	178.41	185.47	337.75
R02	2×10^{-4}	0.5	178.03	188.89	338.93
R03	2×10^{-4}	1.0	178.35	192.62	340.45

This material is declared a work of the U.S. Government and is not subject to copyright protection in the United States.

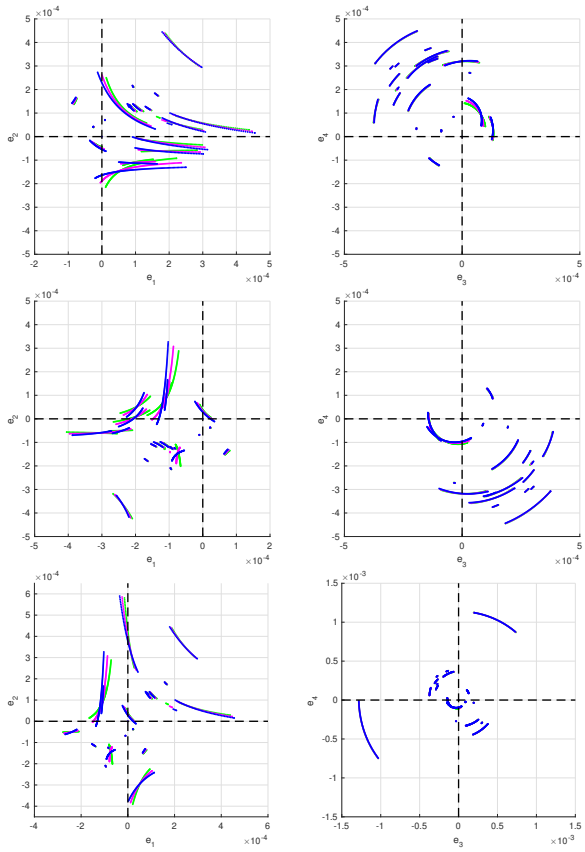

Fig. 14: Projection of Starshade trajectory on the saddle plane $\{e_1, e_2\}$ (left) and center plane $\{e_3, e_4\}$ (right) for cases `R01` magenta, `R02` green, `R03` blue. Top: DRMT trajectory, Middle: DRMA trajectory, Bottom: DRMM trajectory.

6.2 Full DRM with 48 observations

The JPL Starshade team designed a DRM with 48 target stars. For each target star, the Hipparchus (HIP) number, the transfer time between observation, the observation duration, and the sequence of observations were provided [7]. This DRM assumes that all the observations are done for a 2 year time-span starting February 2028 providing a good case to study the cost and viability of the Starshade - WFIRST formation flying at SEL2.

In the previous section we have seen how knowing the relative position in the saddle plane projection can help us understand the effects of changing the SRP coefficients on the total ΔV. In this section we have taken these DRM with 48 observations and performed simulations in the RTBP and a high fidelity modeling tool to verify the results.

6.2.1 RTBP simulations

The DRM provides a list of 48 observations to different target stars with the required slew time between observations and the total observation duration. In STK, an Ideal Starshade (ISH) reference orbit was generated by creating a vector from WFIRST to the target stars in the DRM that was offset from WFIRST by 37,000 km. This Ideal Starshade vector was traced from the desired observation start and stop times listed in the DRM. This vector information was then generated in the RTBP reference frame. Using this Ideal Starshade RTBP vector information, simulations using different SRP models and coefficients for Starshade matching the existing mass and area constraints [1] have been performed.

For WFIRST we have considered a total mass of 8281 kg and an estimated surface area of 49.6 0m^2, having $q_{srp} = 4.6268 \times 10^{-6}$ and $C_r = 2$ for all the simulations. For Starshade we have considered a total mass of 8261 kg and a surface area of 804 m^2, having $q_{srp} = 1.7350 \times 10^{-4}$ and $C_r = 1, 1.1, 1.5, 1.9$ and 2. As extreme cases, and just for comparison, we have also performed one simulation where Starshade has the same area-to-mass ratio and C_r as WFIRST, and another simulation where Starshade is 1000 kg lighter ($q_{srp} = 2.4098 \times 10^{-4}$) and $C_r = 2$.

Simulations using cannonball for SRP

In this section we analyze the results considering the cannonball model for Starshade SRP, using the different area-to-mass ratios and C_r values described above. Table 4 shows the relationship between the total ΔV cost, the sum of the ΔV's of the transfer to beginning of each observation, and the sum of the ΔV's required to reach the end of the observations meeting the ideal location requirement. There we can see how the total cost increases slightly as $C_r \cdot q_{srp}$ increases. For instance, for the same area-to-mass ratio ($q_{srp} = 1.7350 \times 10^{-4}$) from $C_r = 1$ to $C_r = 2$ there is a difference of 2 m/s in the total cost. A larger difference can be seen if we compare case `C19` with `CWF` and `CEX` where the total cost are 1167.24 m/s, 1164.85 m/s and 1170.75 m/s.

Table 4: Total ΔV for the 48 observations taking different C_r values. Simulations in the RTBP model using the cannonball model for SRP.

id	q_{srp}	C_r	ΔV_{trans} [m/s]	$\sum \Delta V_{obs}$ [m/s]	Total ΔV [m/s]
`C10`	1.7350×10^{-4}	1.0	542.37	622.85	1165.21
`C11`	1.7350×10^{-4}	1.1	543.51	621.85	1165.36
`C15`	1.7350×10^{-4}	1.5	548.19	617.95	1166.14
`C19`	1.7350×10^{-4}	1.9	553.05	614.19	1167.24
`C20`	1.7350×10^{-4}	2.0	554.29	613.27	1167.56
`CWF`	4.6260×10^{-6}	2.0	532.14	632.71	1164.85
`CEX`	2.4098×10^{-4}	2.0	564.31	606.44	1170.75

Moreover, Fig. 15 shows the required ΔV to slew to the beginning of each observation (top) and to reach the end of each observation (bottom) only for the cases `C19`, `CWF` and `CEX`. In both, Fig. 15 and Table 4, we can see how as the normalized SRP pressure, $C_r \cdot q_{srp}$, increases the Transfer ΔV cost increases, while the Observation ΔV cost decreases. We can also see that the total ΔV cost increases as $C_r \cdot q_{srp}$ increases.

Let us analyze this from a dynamical point of view. In Fig. 16 we have the XY and YZ projection of WFIRST's reference orbit (blue) and Starshade's trajectory (magenta) where the red points represent the observation locations. Here we can see that Starshade has to go above and below WFIRST throughout the 2 year DRM. But as seen in the previous section, the best way to see

This material is declared a work of the U.S. Government and is not subject to copyright protection in the United States.

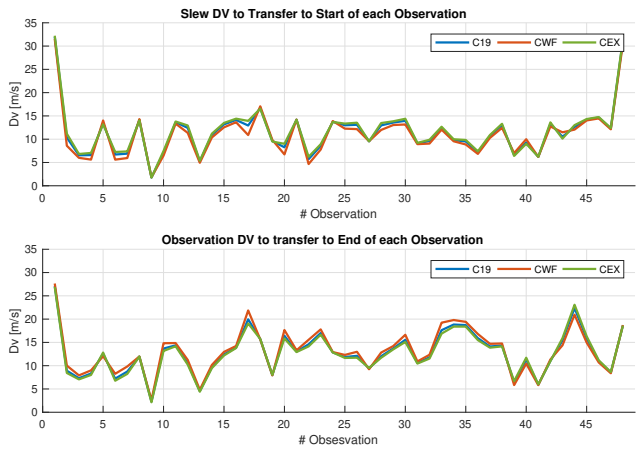

Fig. 15: For the 48 observations. Top: ΔV to slew from the end to start of observation. Bottom: ΔV to reach end of the observation.

how SRP is affecting the trajectory and the cost is to look at the projection of its trajectory in the saddle plane (Fig. 17).

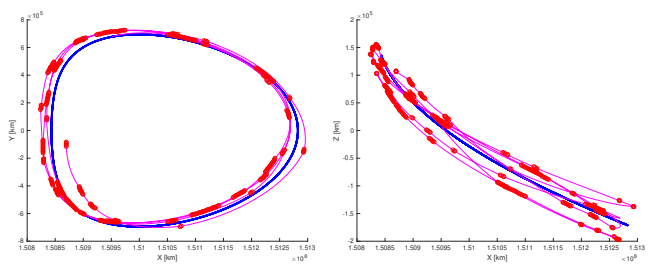

Fig. 16: XY and XZ projection of trajectories for WFIRST (blue) and Starshade (magenta).

Figure 17 shows the projection of this trajectory in the saddle plane. The two plots on the right highlight only the trajectory during the observations, while the two left plots highlight the transfer trajectories. The two plots on the bottom are magnifications on the plots on the top. The color code is used to identify the different cases, where: magenta corresponds to `C19`, green `CWF` and blue `CEX`. Looking at the evolution of the trajectory during the observations (Fig. 17 right) we can see how most of the green lines are longer than the blue and magenta. A larger natural slew can be related with a larger ΔV to control the observation as we have seen in Table 4. Looking at the evolution of the trajectories during the transfer from one observation to the other (Fig. 17 left) we can clearly see the shift of the saddle governing Starshade's motion for the different cases. Looking at the drifts for each transfer trajectory and relating them with the ΔV cost is harder in this case. There are some curves that experience larger excursions than others, and we would need to check each of them individually to see if there is a strict relation.

Simulations using 1-Plate for SRP

In this section we analyze the results considering the 1-plate model for Starshade's SRP. Now the magnitude and direction of the SRP acceleration will depend on Starshade's orientation with respect to the Sun-line. For these simulations we have assumed

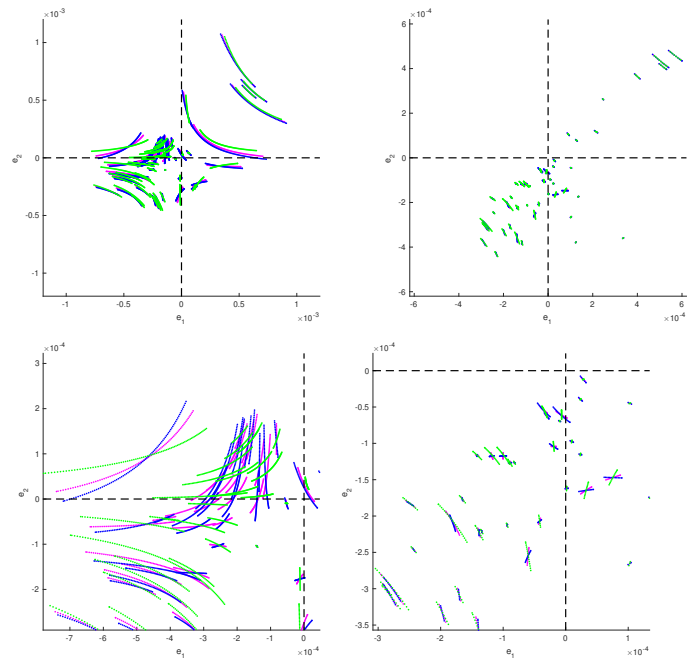

Fig. 17: Projection of Starshade trajectory on the saddle plane $\{\hat{e}_1, \hat{e}_2\}$ for `C19` magenta, `CWF` green and `CEX` blue. Left: Slew trajectories are highlighted. Right: Observation trajectories are highlighted.

that: during the transfer from one observation to the other Starshade's plate is perpendicular to the Sun-line; and during the observations, Starshade's plate is perpendicular to the WFIRST-Star line.

Simulations using this profile for Starshade's attitude have been run, using for $q_{srp} = 1.735 \times 10^{-4}$ and $\rho_s = 0, 0.1, 0.5, 0.9$ and 1. Notice that if Starshade was to be oriented perpendicular to the Sun-line through the whole trajectory, this would correspond to $C_r = 1, 1.1, 1.5, 1.9$ and 1 in the cannonball SRP model. Hence the results we find using these ρ_s values will be good to compare with those in the previous section (Table 4), and study the relevance of the plate reflectivity properties.

Table 5 shows for different ρ_s values, the total ΔV cost, the sum of the ΔV's to transfer Starshade to the beginning of each observation, and the sum of the ΔV's required to reach the end of the observations meeting the ideal location requirement. There we can see how increasing the reflectivity (making it more solar sail like) actually decreases the total ΔV, whereas before, there is a difference of only 2 m/s between the two extreme cases $\rho_s = 0$ and $\rho_s = 1$.

Figure 18 shows the cost of the individual 48 observations for $\rho_s = 0, 0.5$ and 1. The top plot shows the ΔV for slewing from one observation to the other, while the bottom plot shows the required ΔV to reach the end of the observation. We can see a similar behavior as in Fig. 15 but with smaller variations as we are considering same q_{srp} cases.

Figure 19 shows WFIRST (blue) and Starshade (magenta) trajectories in the RTBP reference frame during the 2 years of observations. Again the red points represent the location of Starshade

This material is declared a work of the U.S. Government and is not subject to copyright protection in the United States.

Table 5: Total ΔV for the 48 observations taking different C_r values. Simulations in the RTBP model using the plate model for SRP.

id	q_{srp}	ρ_s	ΔV_{trans} [m/s]	$\sum \Delta V_{obs}$ [m/s]	Total ΔV [m/s]
P00	1.7350×10^{-4}	0.00	540.20	622.09	1162.28
P01	1.7350×10^{-4}	0.10	540.94	621.02	1161.97
P05	1.7350×10^{-4}	0.50	544.03	616.98	1161.01
P09	1.7350×10^{-4}	0.90	547.25	613.28	1160.53
P10	1.7350×10^{-4}	1.00	548.08	612.41	1160.49

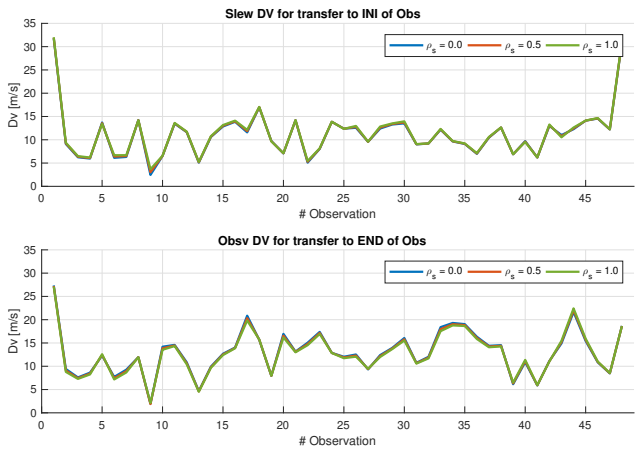

Fig. 18: For the 48 observations. Top: ΔV to slew to reach the start of the next observation. Bottom: ΔV to reach end of the observation.

during the observations. Here we include the normal direction to Starshade's plate (**n**) for illustrative purposes.

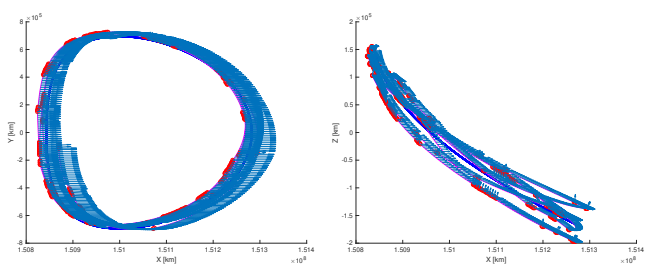

Fig. 19: XY and XZ projection of trajectories for WFIRST (blue) and Starshade (magenta). The blue arrows corresponds to the normal direction to Starshade's plate (**n**).

In order to analyze the effects of changing the reflectivity properties on Starshade's dynamics, we look at the projection of its trajectory on the saddle plane (Fig. 20). There we can see the projection of three different cases P00 magenta, P05 blue and p10 green for the transfer trajectories (left) and the observations (right). Notice that changes on the reflectivity coefficient ρ_s have similar effects as changing C_r for the cannonball model, i.e. the saddle location is displaced and this can affect the total cost. Table 5 shows a difference of only 2 m/s in the total cost, and as we can see in Fig. 20 there are no drastic differences in the shape of the trajectories for the different ρ_s coefficients.

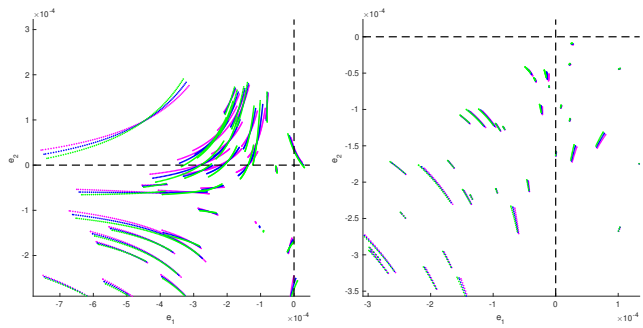

Fig. 20: Projection of Starshade's trajectory on the saddle plane $\{\hat{e}_1, \hat{e}_2\}$ for P00 magenta, P05 blue and p10 green. Left: Only the slew trajectories. Right: Only the observation trajectories.

6.2.2 High-fidelity simulations

Using MATLAB and the automated process called STK COM, the file containing the 48 observation DRM information can be read and processed in STK, which has an internal star catalog, and using the HIP number the different stars can be included in an STK scenario. Then an Ideal Starshade (ISH) reference orbit is generated by creating a vector from WFIRST's reference position to the target stars in the DRM that is 37,000 km offset from WFIRST.

With the ISH spacecraft, the start and end of each observations can be taken and turned into target locations to use in a Differential Corrector. A separate spacecraft for Starshade-Occulter is created to propagate between each observation, and to calculate a maneuver to target the start and end position of each observation [16]. To simplify the overall simulation initialization, the Starshade-Occulter begins in a similar orbit as WFIRST, and performs a small impulsive maneuver to separate itself from WFIRST. A second impulsive maneuver is done to target the starting position relative to WFIRST for the first observation using the defined slew time in the DRM. Once "Starshade Occulter" reaches the start position for the observation, another impulsive maneuver is performed to target the end position for the observation using the defined observation time in the DRM. Once the end state is reached, Starshade-Occulter repeats this sequence to move to the start of the next observation until the observation sequence is finished.

Figure 21 shows the trajectories of WFIRST (magenta) and Starshade (green) after the full 2 year simulation, where we can appreciate their relative position throughout the mission. Figure 22 presents a closer look at the relative positions of the two spacecrafts during observation 41. There we can see how WFIRST, Starshade and star are aligned.

Table 6 shows the total ΔV for the different cases that have been analyzed. We note that these cases are the same as the ones presented in Section 6.2.1 using the cannonball model and that are summarized in Table 4. Comparing both tables one can see that the effect of changing C_r or the area-to-mass ratio for Starshade (cases CWF and CEX) have the same effect in both simulations. The difference in the total cost can be due to the difference in

This material is declared a work of the U.S. Government and is not subject to copyright protection in the United States.

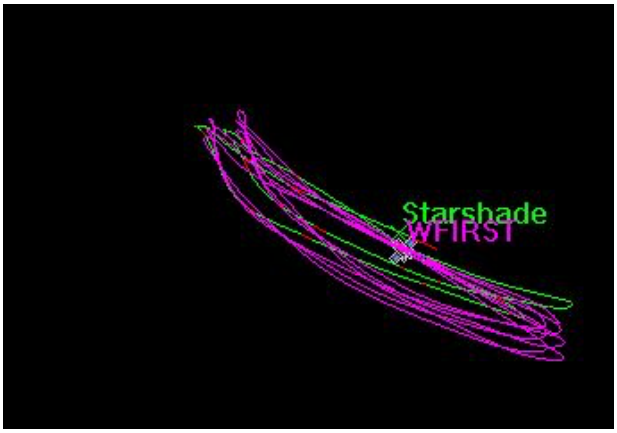

Fig. 21: XZ projection of WFIRST (magenta) and Starshade (green) trajectories for the 48 observation DRM simulation in STK.

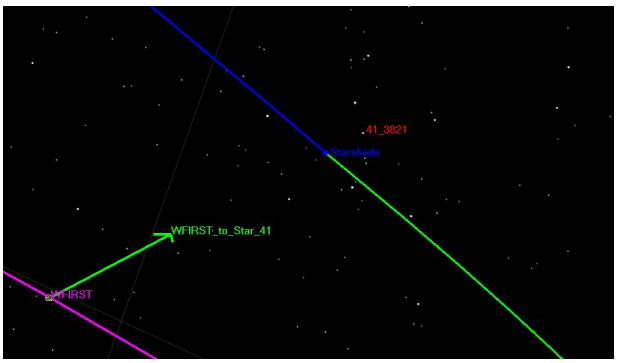

Fig. 22: Relative position of WFIRST, Starshade and Star during observation 41.

the dynamical model and small differences in the starting date. But the results are consistent enough to consider the simulations in the RTBP model good insight into how SRP is affecting the motion of Starshade relative to WFIRST and the ΔV cost.

Table 6: Total ΔV for the 48 observations taking different C_r values. Simulations using STK and the cannonball model for SRP.

id	Dry Mass (kg)	Fuel Mass (kg)	SRP Area (m^2)	C_r	Total ΔV [m/s]
C10	1400	1171	804	1.0	1140.9
C11	1400	1171	804	1.1	1141.3
C15	1400	1171	804	1.5	1143.2
C19	1400	1171	804	1.9	1145.6
C20	1400	1171	804	2.0	1146.3
CWF	7344	937	49.6	2.0	1139.4
CEX	1000	571	804	2.0	1156.8

Figure 23 shows shows the required ΔV to slew to the beginning of each observation (top) and to reach the end of each observation (bottom) for the cases C19, CWF and CEX.

It is important to note that the maneuvers are being executed to achieve the start and end of each observation, only meant to help with initial Starshade design aspects. There is no active maneu-

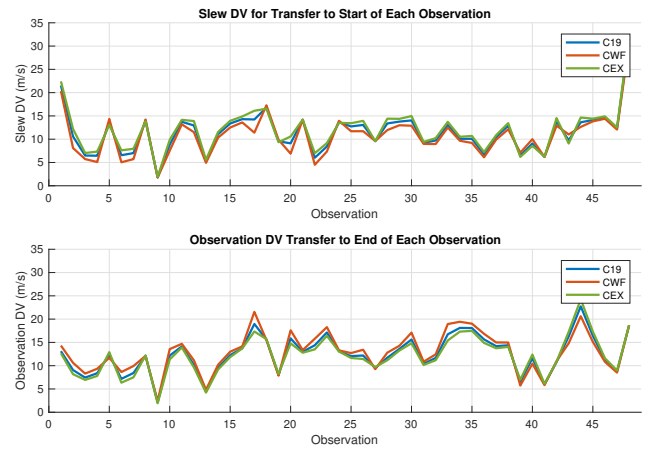

Fig. 23: For the 48 observations simulations in STK. Top: ΔV to slew from the end to start of observation. Bottom: ΔV to reach end of the observation.

vering or control done between the start and end of the observation, and Starshade is allowed to drift naturally during the observation time. We leave as future work the study on the required ΔV to actively hold Starshade along the line of sight during the observation.

However, to help provide some insight into how much control will be required to keep Starshade aligned with WFIRST during the observation, we have looked at the angular variation of Starshade off the line of sight and the drift of Starshade during the observation in this previous simulation. We note that Starshade is allowed to vary in the radial distance along the line of sight, but must not move laterally off the line of sight during an observation. The top plot in Fig. 24 shows the radial variation between WFIRST and Starshade for simulations C19. Here we can see that for most of the observations the radial distance variation is less that 50 km, and the maximum drifts are of 175.4 km away from WFIRST and 99.4 km towards WFIRST. The bottom plot in Fig. 24 shows the angle between the vectors joining WFIRST and Starshade and WFIRST and Ideal Starshade. This angle represents the separation of Starshade off the desired line of sight during an observation (and hence provides insight into how much Starshade moves in the lateral direction without control). Notice that this variation is always less that $0.4°$. Despite this angle being small, at a distance of 37,000 km, a displacement of $0.4°$ corresponds to a misalignment of 258 km with respect to the line of sight. Hence, a control sequence to keep Starshade aligned with WFIRST during observations will be required.

7 Conclusions and Future Work

In this paper we have analyzed the formation flying of two spacecraft, a telescope and an occulter at the SEL2 vicinity. The study focuses on WFIRST and Starshade, but the analysis is general enough to consider other spacecrafts with similar constraints. A dynamical explanation using the Floquet Modes reference frame around a reference Halo orbit for WFIRST has been provided.

This material is declared a work of the U.S. Government and is not subject to copyright protection in the United States.

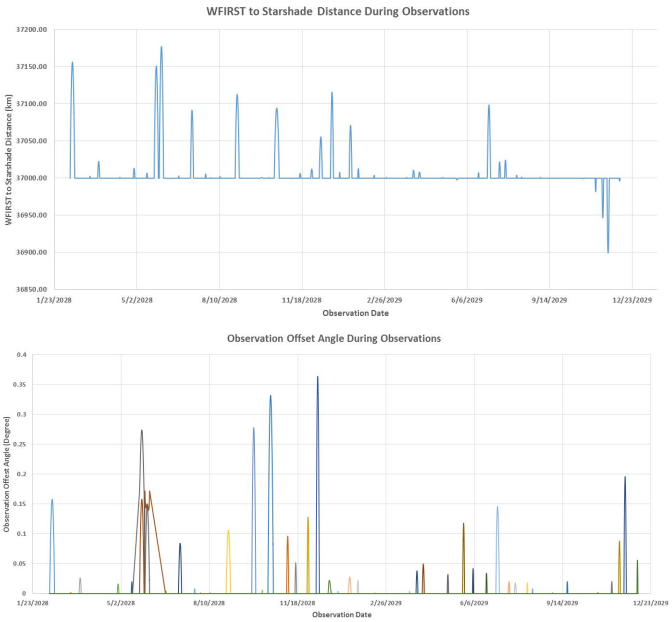

Fig. 24: Top: Variation of Starshade - WFIRST radial distance during the observations. Bottom: Angular displacement from Ideal Starshade - WFIRST line for each observation.

This approach allows us to understand if there are privileged locations for Starshade relative to WFIRST which reduces the total ΔV for the formation flight concept.

Section 6.1 provides an analysis on the relation between the relative location of the observations with respect to WFIRST in the saddle projection of the trajectory, where it has been shown that concentrating all the observations within the same region in the phase space helps reduce the overall cost. Moreover, it has been shown that observations that require Starshade to be closer to the Sun than WFIRST are less sensitive to changes in the area-to-mass ratio and the reflectivity coefficients, than observations where Starshade is further away from the Sun than WFIRST. This can be something to take into account when selecting the sequence of stars or the order in which they are observed.

Section 6.2 analyses a DRM with 48 observations provided by the JPL Starshade group and how changes in the SRP coefficients affect the total ΔV. Simulations in the RTBP and with a higher-fidelity model have been performed, validating the results provided by the RTBP. This gives us confidence in the dynamical explanation provided by looking at the projections of the trajectory in the saddle and center of the Floquet Modes reference frame.

In the higher-fidelity simulations done in STK the displacement between the Ideal Starshade location and the simulated Starshade location has been computed for each of the 48 observations. The radial displacements observed were under 200km, however large misalignment in the line of sight for some of the observations were observed, specially those that require more time. Hence, a control strategy is required to ensure there is no misalignment between Starshade and WFIRST during the observations.

Acknowledgments

The work has been funded under the Goddard Planetary Heliophysics Institute Task 595.001 in collaboration with the University of Maryland Baltimore County (UMBC) under the NNG11PL02A.

References

[1] S. Seager, K. Warfield, W. Cash, S. Domagal-Goldman, N. J. Kasdin, M. Kuchner, A. Roberge, S. Shaklam, W. Sparks, M. Thomson, M. Turnbull, D. Lisman, R. Baran, R. Bauman, E. Cady, C. Henegham, S. Martin, D. Scharf, R. Trabert, D. Webb, P. Zarifian, "Exo-S: Starshade Probe-Class Exoplanet Direct Imagining Mission Concept Final Report". March 2015.

[2] L. Millard, K. Howell, "Optimal reconfiguration maneuvers for spacecraft imaging arrays in multi-body regimes." *A*cta Astronautica, Volume 63, Issues 11-12, pp 1283-1298, December 2008.

[3] Vallado, D. "Fundamentals of astrodynamics and applications", McGraw-Hill Companies, Inc, New York, 1997.

[4] M. Ziebart, "High precision analytical solar radiation pressure modelling for GNSS spacecraft", PhD Dissertation, University of East London, 2001.

[5] M. Ziebart, "Generalized Analytical Solar Radiation Pressure Modeling Algorithm for Spacecraft of Complex Shape", *J*ournal of Spacecraft and Rockets, Volume 41, No. 5, 2004.

[6] A. Farres, C. Webster, D. Folta, "High fidelity modeling of SRP and its effect on the relative motion of Starshade and WFIRST", *A*IAA SciTech Forum, 2018 Space Flight Mechanics Meeting, January 2018, Kissimee, FL, United States.

[7] C. Webster, D. Folta, "IWSCFF 17-74: Understanding the Sun-Earth Libration Point Orbit Formation Flying Challenges for WFIRST and Starshade", *9*th International Workshop on Satellite Constellations and Formation Flying, June 2017, Boulder, CO.

[8] A. Farres; D. Folta D.; Webster C.; "Using Spherical Harmonics to model Solar Radiation Pressure Accelerations", *A*AS/AIAA Astrodynamics Specialist Conference, Columbia River Gorge, Stevenson, WA, August 20-24, 2017.

[9] A. Farres, A.; Jorba, À.; "Periodic and Quasi-Periodic Motion of a Solar Sail close to SL1 in the Earth-Sun System", *C*elestial Mechanics and Dynamical Astronomy, Volume 107, num. 1-2, pp. 233-253, June 2010.

[10] A., Farres; "Catalogue on the Dynamics of a Solar Sail around L1 and L2", *Proceedings of the 4th International*

This material is declared a work of the U.S. Government and is not subject to copyright protection in the United States.

Symposium on Solar Sailing, Kyoto, Japan, 17-20 January 2017.

[11] A. Farres, C. Webster, J. Donaldson, D. Folta, "*O*rbital Maintenance for the Wide Field Ifrared Survey Telescope: The Effects of Solar Radiation Pressure and Navigation Accuracies on Station Keeping", 2018 AAS/AIAA Astrodynamics Specialist Conference, Snowbird, Utah.

[12] G. Gòmez, J. Llibre, R. Martinez, C. Simó, "Dynamics and mission design near libration points - Volume I: fundamentals: the case of collinear libration points", *W*orld Scientific Monograph Series in Mathematics, Vol. 2, World Scientific, 2001.

[13] C. Simó, G. Gòmez, J. Llibre, R. Martinez, J. Rodriguez, "Station Keeping of Quasiperiodic Halo Orbits Using Invariant Manifolds", *S*econd International Symposium on Spacecraft Flight Dynamics, ESA, pp. 65-70, 1986.

[14] Farres, A., Jorba. A., "Station keeping of a solar sail around a Halo orbit", Acta Astronautica Volume 94, Issue 1, pp. 527-539, January-February 2014.

[15] Farres, A., Jorba, A., "A Dynamical System Approach for the Station Keeping of a Solar Sail", The Journal of the Astronautical Science, Volume 56, Number 2, pp. 199-230, April-June 2008.

[16] Folta, D., Lowe, J., "Formation Flying of a Telescope/Occulter system with large separations in an L2 Libration Orbit", *5*9th International Astronautical Congress, Glasgow, Scotland, September-October 2008.